Engineering Science and Technology, an International Journal 36 (2022) 101168

HOSTED BY

Contents lists available at ScienceDirect

Engineering Science and Technology, an International Journal

journal homepage: www.elsevier.com/locate/jestch

Full Length Article

Effect of reverse-polarity hot wire on the tandem arc welding process

Jin-young Kim, Juyeong Lee, Seung Hwan Lee *

Department of Mechanical Engineering, Hanyang University, 222 Wansimni-ro, Seongdonggu, Seoul 04763, Republic of Korea

ARTICLE INFO

Article history:
Received 19 January 2022
Revised 6 April 2022
Accepted 20 April 2022

Keywords:
Hot wire
Molten pool
Numerical simulation
Arc interaction
Level-set method
Magneto-hydrodynamics

ABSTRACT

A novel three-dimensional two-step numerical model was developed and analyzed for a tandem process with a reverse-polarity hot wire. Magneto-hydrodynamic analysis was conducted and the free surface of the molten pool was tracked to investigate the arc and molten pool behaviors of the proposed process, respectively. The results indicated that a change in electromagnetic force by the hot wire reduced arc deflection, which increased the arc velocity in the co-axial direction of electrodes, thereby increasing the arc pressure and arc shear force acting on the molten pool. Consequently, the molten pool in the novel tandem process was wider and deeper than that in the conventional tandem process.

1. Introduction

The tandem arc welding process is typically used in heavy industries, such as shipbuilding and construction industries, because of its high productivity, deposition rate, and welding speed [1–3]. To increase the effectiveness of welding in these industries, methods involving the application of a higher current or the use of more electrodes have been considered. However, the weld quality of such methods is inferior because the molten pool becomes unstable because of arc interaction caused by high current and multiple electrodes.

Numerous processes have been proposed to address this molten pool stability problem caused by arc interaction [4–6,21]. Arita et al. [4] first proposed the H-tandem process in which a reverse-polarity hot wire was added between two electrodes in the tandem MAG fillet welding conducted using a zinc coated steel plate. They reported that compared with the conventional tandem process, the addition of reverse-polarity hot wire reduced arc interaction between tandem electrodes and increased the viscosity of the molten pool because of the reduction in temperature. Yokota et al. [5] revealed that weldments with sound bead appearance and low porosity can be obtained at a high welding speed of 2.0 m/min in the H-tandem process because of the higher molten pool stability and arc interaction resistance. Lee et al. [6,21] investigated process parameter optimization and obtained a high welding quality in the H-tandem MAG welding process of the AH36 plate. They optimized parameters, such as the current and voltage of each electrode, hot wire feed rate, and interwire distance (IWD), and proposed a combination of process parameters, such as the leg length, penetration, and convexity, for the optimal welding quality by assigning weights to indicate welding quality. Furthermore, they reported that the leading current and voltage and the hot wire current considerably influence welding quality.

In the aforementioned H-tandem process, a numerical model for the conventional tandem process is required to identify mechanisms for changes in arc and molten pool behavior that are caused by hot wire. Magneto-hydrodynamic (MHD) analysis is required to analyze arc and molten pool behavior in the tandem process. Wu et al. [7] developed an MHD-based numerical model for high-speed tandem TIG welding, in which a pure titanium thin plate is used to investigate arc and molten pool behavior. They revealed that the molten pool flowed downwards and backwards under the leading electrode and downwards and forwards under the trailing electrode. They revealed that the pull–push flow pattern, defined as the backward molten pool flow after the leading electrode and forward molten pool before the training electrode, occurs because of the Marangoni effect and arc shear stress. Ogino et al. [8] developed a MHD-based numerical model for the tandem TIG welding process, in which SUS304 was used to investigate arc plasma, molten pool behavior, and flow of the molten pool under the influence of electromagnetic force, arc force, and the Marangoni effect. They determined that the molten pool is elliptical because of arc interaction, and the flow rate in the width direction of the molten pool is slower and the penetration depth is higher in

* Corresponding author.
E-mail address: seunghlee@hanyang.ac.kr (S.H. Lee).
Peer review under responsibility of Karabuk University.

https://doi.org/10.1016/j.jestch.2022.101168

Nomenclature

ρ	Density (kg/m^3)	$\boldsymbol{q}$	Heat flux (W/m^2)
t	Time (s)	q_{conv}	Convective heat flux (W/m^2)
p	Pressure (Pa)	q_{rad}	Radiative heat flux (W/m^2)
p_0	Reference pressure (Pa)	h_c	Convective heat coefficient $(W/(m^2 \cdot K))$
μ	Dynamic viscosity (Pa/s)	σ_s	Stefan-Boltzmann constant $(W/(m^2 \cdot K^4))$
μ_g	Dynamic viscosity of argon (Pa/s)	ε	Emissivity
$\boldsymbol{g}$	Gravitational acceleration vector (m/s^2)	Q_i	Heat input (W)
V_{sub}	Welding speed (m/s)	r_{af}	Characteristic radius of flux distribution in the front x direction (m)
C	Constant	r_{ar}	Characteristic radius of flux distribution in the rear x direction (m)
λ	Constant	r_b	Characteristic radius of flux distribution in the y direction (m)
α	Volume fraction of the liquid phase	r_c	Characteristic radius of flux distribution in the z direction (m)
$\boldsymbol{F}$	Body force term (N/m^3)	f_f	Fraction of the heat deposited in the front quadrants
$\boldsymbol{F_{SLD}}$	Solid force term (N/m^3)	f_r	Fraction of the heat deposited in the rear quadrants
$\boldsymbol{F_{EM}}$	Electromagnetic force term (N/m^3)	l	Lag factor (m)
σ	Electrical conductivity (S/m)	$\boldsymbol{\tau}$	Shear stress (Pa)
V	Electrical potential (V)	γ	Surface tension coefficient (N/m)
$\boldsymbol{A}$	Magnetic potential (Wb/m)	ϕ	Level-set variable
$\boldsymbol{J}$	Current density (Pa)	γ_{ls}	Reinitialization parameter (m/s)
$\boldsymbol{B}$	Magnetic flux density (T)	ϵ_{ls}	Parameter controlling interface thickness (m)
W	Heat source by joule heating (m/s)	κ	Curvature $(1/m)$
T	Temperature (K)	$\boldsymbol{n}$	Normal vector component
T_0	Reference temperature (K)		
T_L	Liquidus temperature (K)		
T_S	Solidus temperature (K)		
C_p	Specific heat capacity at constant pressure $(J/(kg \cdot K))$		
k	Thermal conductivity $(W/(m \cdot K))$		
Q	Heat source term (W/m^3)		

the tandem welding process than those in the single TIG welding process because the shear stress caused by plasma is low.

Because the electromagnetic force, arc pressure, and surface shear force calculated through the MHD analysis function as driving forces on the molten pool flow, considering changes in the free surface of the molten pool is critical for the accurate analysis of the molten pool behavior mechanism [9,10]. The following studies performed MHD analysis with the free surface tracking analysis of the molten pool. Wang et al. [9] developed an analysis model in which the MHD analysis with the level-set method was used for tracking the free surface of the molten pool in pulsed-GTAW process by using SUS304 steel. Their model is suitable for analyzing the mechanism of the GTAW process, and pulsed current are used for predicting the geometry of the molten pool. Cadiou et al. [10] implemented the geometry of the molten pool in the wire arc additive manufacturing process of STS304 by combining the three-dimensional MHD analysis with the level-set method. Their model can simulate the growth of the molten pool and the evolution of the temperature and velocity fields of the molten pool during the deposition process. A numerical model that combines MHD analysis with tracking of the free surface of the molten pool is required to analyze the mechanism of molten pool behavior. However, in numerical models, combining MHD with free surface tracking of the molten pool is difficult in processes, such as the tandem and H-tandem processes, with multiple electrodes because considerable computing resources and calculation times are required.

In this study, a novel three-dimensional (3D) numerical MHD analysis model with free surface tracking analysis of the molten pool was developed to analyze the novel H-tandem process with a reverse-polarity electrode. The reverse-polarity hot wire was added to the two electrodes in the tandem process for the reduction of arc interaction. The developed model is a two-step process in which arc behavior and the forces acting at the surface of the base metal are calculated through MHD analysis, and the free surface of the molten pool is tracked through the level-set method. Furthermore, the molten pool behavior is implemented considering the forces acting on the free surface. This model was used to analyze the forces acting on the arc and molten pool and the mechanisms for changes in molten pool behavior under such forces in the tandem and H-tandem processes. The developed two-step model significantly reduced the computation time and effectively analyzed the mechanisms of arc and molten pool behavior compared to the model that considers all physics simultaneously. The results of each process were validated by comparing them with the weld cross-sections obtained using the welding experiments under the same process conditions.

2. Mathematical models

In the first step of the two-step model, the MHD system was used for analyses under the moving base metal and fixed electrodes (leading and trailing electrodes and hot wire). In step 2, the behavior of the molten pool on applying the heat source and forces was observed, as displayed in Fig. 1. In step 1, MHD analysis was performed to calculate the electromagnetic force resulting from the current applied to each electrode, the heat by Joule heating, and the pressure and surface shear force acting at the surface of the base metal. In step 2, the free surface of the molten pool was tracked through the level-set method, and the behavior of the molten pool were calculated using the analysis results from step 1. To simulate 2 s of the process, computation time was expected to take months on 32 cores and 192 GB RAM when the MHD and free surface tracking analysis are considered simultaneously. However, the computation time was shortened to about 10 days using the developed two-step model. COMSOL 5.5, a commercial software, was used for the numerical analysis of the tandem and H-tandem processes.

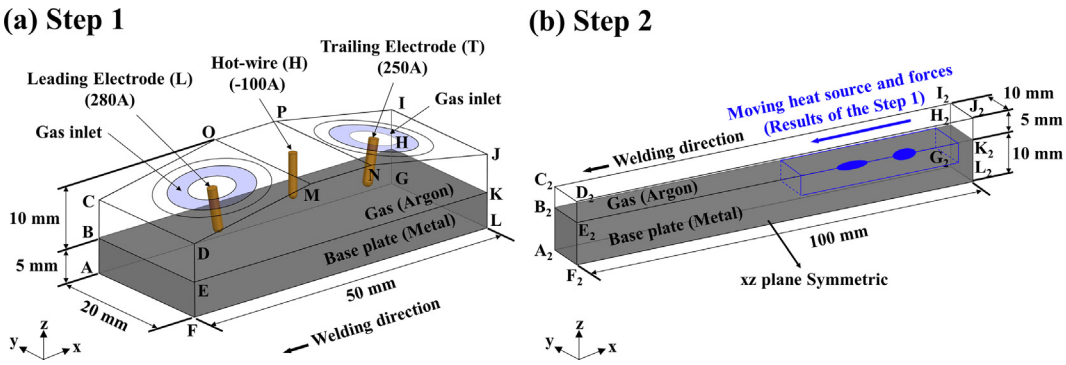

Fig. 1. Computational domain in the numerical model for H-tandem welding simulation.

2.1. Step 1: Arc model

In step 1, the diameter of the leading and trailing electrodes and the hot wire were 1.4 and 1.2 *mm*, respectively. IWD for the leading and trailing electrodes was 25 *mm*, and hot wire was in the center between the two electrodes. The travel angles of the leading and trailing electrodes and hot wire were 10°, −10°, and 0° with respect to the yz-plane. The currents applied to the leading and trailing electrodes, 280 *A* and 250 *A*, respectively, were the same for both tandem and H-tandem processes. In the H-tandem process, the hot wire with a reverse polarity was added, and the applied current was −100 *A*. Because this study analyzed the change in electromagnetic force caused by the hot wire, droplet transfers were not considered. All gas regions were assumed to be Ar regions, which was used as the shielding gas. The contact tip to work distance (CTWD) of the leading and trailing electrodes were 18 *mm* and 21 *mm* respectively. The flow rate of the shielding gas at the nozzle end was 18 *L/min* for the two electrodes. Therefore, due to the difference of the CTWD between the electrodes, the flow rate of the shielding gas entering the control volume was set to 7.8 *L/min* and 1.45 *L/min* for each leading and trailing region, respectively. These values were derived in previous simulations. The vaporization of the molten metal was neglected, and the thermal effect at the anode and cathode plasma interface because of the decrease in the voltage was also neglected. Considerable computation load and time are required to detail the movement of electrodes or the solid base metal. Therefore, the base metal was assumed to be a liquid phase and set to flow in at a speed of 1.0 *m/min* in front of the leading electrode and flow out behind the trailing electrode [10]. No deformation was assumed to occur at the interface between gas and liquid, which was the surface of the base metal. The gas and liquid were laminar flows and assumed to be immiscible and incompressible Newtonian fluids.

The element size was 0.3 *mm* at the interfaces between the gas and each electrode and at the gas–liquid interface. The element in the remaining regions was set to gradually become coarse from these interfaces. Previously reported thermal conductivity, electrical conductivity, and dynamic viscosity of Ar [11,12], which are dependent on the temperature, were used. Table 1 lists the material properties of the base metal. The ground condition was set on the AGLF surface, and the slip condition was set on the AGLF, ABHG and EKLF surfaces. Furthermore, the base metal flowed in through the ABEF surface and flowed out through the GHKL surface. For the remaining interfaces, the outflow condition was set. Table 2 is the boundary conditions of step 1 model.

The governing equations of step 1, mass, momentum, and energy conservation equations are as follows:

$$\frac{\partial \rho}{\partial t} + \nabla \cdot (\rho \boldsymbol{u}) = 0 \tag{1}$$

Table 1
Material properties of AH36 steel.

Nomenclature	Value	Nomenclature	Value
Density (kg/m^3)	7200	Latent heat of fusion (J/kg)	247
Dynamic viscosity $(Pa \cdot s)$	0.006	Liquidus temperature (K)	1800
Specific heat (liquid) $(J/(kg \cdot K))$	866	Solidus temperature (K)	1750
Specific heat (solid) $(J/(kg \cdot K))$	686	Coefficient of thermal expansion (K^{-1})	1×10^{-4}
Thermal conductivity (liquid) $(W/(m \cdot K))$	26.0	Electrical conductivity (S/m)	7.7×10^5
Thermal conductivity (solid) $(W/(m \cdot K))$	32.3		

Table 2
Boundary conditions of step 1 model for H-tandem model.

Area	Electromagnetic	Flow	Heat transfer
AGLF	$\boldsymbol{V} = 0, \boldsymbol{n} \times \boldsymbol{A} = 0$	$\boldsymbol{u} \cdot \boldsymbol{n} = 0$	$T = T_0$
ABHG, EKLF	$\boldsymbol{n} \cdot \boldsymbol{J} = 0, \boldsymbol{n} \times \boldsymbol{A} = 0$	$\boldsymbol{u} \cdot \boldsymbol{n} = 0$	$T = T_0$
ABEF	$\boldsymbol{n} \cdot \boldsymbol{J} = 0, \boldsymbol{n} \times \boldsymbol{A} = 0$	$u = V_{sub}$	$T = T_0$
BCDE, COMD, OPNM, PIJN, HIJK, DMNJKE, BCOPIH	$\boldsymbol{n} \cdot \boldsymbol{J} = 0, \boldsymbol{n} \times \boldsymbol{A} = 0$	$\partial(\rho \boldsymbol{u})/\partial x = 0$ $\partial(\rho \boldsymbol{v})/\partial y = 0$ $\partial(\rho \boldsymbol{w})/\partial z = 0$	$\boldsymbol{n} \cdot \boldsymbol{q} = 0$
GHKL	$\boldsymbol{n} \cdot \boldsymbol{J} = 0, \boldsymbol{n} \times \boldsymbol{A} = 0$	$u = V_{sub}$	$\boldsymbol{n} \cdot \boldsymbol{q} = 0$

$$\rho \frac{\partial \boldsymbol{u}}{\partial t} + \rho(\boldsymbol{u} \cdot \nabla)\boldsymbol{u} = \nabla \cdot \left[-p\boldsymbol{I} + \mu\left(\nabla \boldsymbol{u} + (\nabla \boldsymbol{u})^T\right)\right] + \boldsymbol{F} + \rho \boldsymbol{g} \tag{2}$$

$$\rho C_p \frac{\partial T}{\partial t} + \rho C_p \boldsymbol{u} \cdot \nabla \boldsymbol{T} = \nabla \cdot (k \nabla T) + Q \tag{3}$$

where ρ is the density, t is the time, $\boldsymbol{u}$ is the velocity component, p is the pressure, μ is the dynamic viscosity, and $\boldsymbol{g}$ is the gravitational acceleration. Furthermore, C_p is the specific heat, T is the temperature, k is the thermal conductivity, $\boldsymbol{F}$ in Eq. (2) is a body forces term, which includes electromagnetic force and solid force. Here, $\boldsymbol{F_{EM}}$, which is the electromagnetic force generated by the current applied to the electrodes, is calculated as $\boldsymbol{J} \times \boldsymbol{B}$, where $\boldsymbol{J}$ is the current density and expressed as $\boldsymbol{J} = -\sigma \nabla V$. Moreover, σ is the electrical conductivity, V is the electric potential, and $\boldsymbol{B}$ is the magnetic field and expressed as $\boldsymbol{B} = \nabla \times \boldsymbol{A}$, where $\boldsymbol{A}$ is the magnetic vector potential. Q in Eq. (3) is a heat source term which is caused by joule heating, convection, and radiation. Joule heating W is caused by current density and electrical resistance and expressed as $W = |\boldsymbol{J}|^2/\sigma$. Because the region with a temperature lower than the melting point in the metal assumed to be liquid must be treated as the solid phase, all behavior should be constrained, with the exception of

the flow in the welding direction. The solid force to express a metal assumed to be liquid, $\boldsymbol{F_{SLD}}$ [10,13,14], is as follows:

$$\boldsymbol{F_{SLD}} = -\frac{C(1-\alpha)^2}{(\alpha^3+\lambda)}(\boldsymbol{u}-\boldsymbol{V_{sub}}) \tag{4}$$

where C is set as 1×10^4 to suppress the velocity in the solid region, and λ is set as 1×10^{-3} to avoid division by zero, respectively. Here, $\boldsymbol{V_{sub}}$ is the velocity in the welding direction of the metal in the liquid and solid phases, α is a variable that represents solid–liquid phase transformation to distinguish the liquid and solid phases of the metal and is expressed as follows:

$$\alpha = \begin{cases} 1, & if\ \ T > T_L \\ \frac{T-T_S}{T_L-T_S}, & if\ \ T_S \le T \le T_L \\ 0, & if\ \ T < T_S \end{cases} \tag{5}$$

where T_L and T_S are the liquidus and solidus temperatures of the metal. The material properties change linearly by the α value which is dependent on the temperature.

In the step 1 model, the governing equations of electromagnetic, heat transfer, and fluid flow are then consecutively and iteratively solved by PARDISO direct solver. Time-dependent study is conducted in this step, and the implicit time-stepping based on the backward differentiation formulas is applied.

2.2. Step 2: Molten pool model

As displayed in Fig. 1(b), the pressure, surface shear force, electromagnetic force, and heat source acting on the base metal calculated in step 1 were applied to the step 2 model. The pressure and surface shear force were applied to the free surface of the molten pool tracked using the level-set method in step 2 as boundary conditions, and the electromagnetic force was applied as the volume force of the molten pool region. A relatively large value of viscosity was applied to suppress the velocity in the solid region. The analysis domain was a symmetric model with respect to the xz-plane.

The minimum element size of the numerical model was 0.3 *mm* at the gas–liquid interface, and it was set to become gradually coarse from this interface for the remaining regions. Convection and radiation conditions to the outside were considered for the boundaries $A_2B_2E_2F_2$, $G_2H_2K_2L_2$, $E_2K_2L_2F_2$ and $A_2B_2H_2G_2$, whereas the open boundary condition was applied to the remaining boundaries to set free fluid flow inside and outside the domain. Table 3 is the boundary conditions of step 2 model.

The heat source was modelled as a double-ellipsoidal shape in the step 2 model and applied to the metal. These heat sources were modelled according to Goldak's model, in which the heat input to the base metal surface is calculated through MHD analysis in consideration of Joule heating in step 1 and used as heat sources in step 2. The Goldak's double ellipsoidal model is expressed as follows [15]:

$$q(x,y,z,t) = \frac{6\sqrt{3}f_f Q_i}{r_{af} r_b r_c \pi\sqrt{\pi}} e^{-3[x+V_{sub}(l-t)]^2/r_{af}^2} e^{-3y^2/r_b^2} e^{-3z^2/r_c^2} \tag{6}$$

$$q(x,y,z,t) = \frac{6\sqrt{3}f_r Q_i}{r_{ar} r_b r_c \pi\sqrt{\pi}} e^{-3[x+V_{sub}(l-t)]^2/r_{ar}^2} e^{-3y^2/r_b^2} e^{-3z^2/r_c^2} \tag{7}$$

Table 3
Boundary conditions of step 2 model for H-tandem model.

Area	Flow	Heat transfer
$A_2B_2E_2F_2$, $G_2H_2K_2L_2$, $E_2K_2L_2F_2$, $A_2B_2H_2G_2$	$u=0, v=0, w=0$	$q_{conv} = -h_c(T-T_0)$ $q_{rad} = -\sigma_s\hat{\varepsilon}\left(T^4-T_0{}^4\right)$
$B_2C_2D_2E_2$, $H_2I_2J_2K_2$, $D_2J_2K_2E_2$, $B_2C_2I_2H_2$	$p = p_0$	$\boldsymbol{n}\cdot\boldsymbol{q} = 0$

where r_{af}, r_{ar}, r_b, r_c are the characteristic radius of flux distribution in x, −x, y, z direction each. These parameters were determined from the effective region of the double-ellipsoidal heat source for each electrode. The position of the maximum heat flux q_{max} of each region calculated from the surface of the base metal in the step 1 model was defined as the center of the double-ellipsoidal heat source. The region at which the heat flux was greater than the heat flux of q_{min} was defined as an effective region of the double-ellipsoidal heat source, where $q_{min} = 0.01\times q_{max}$. f_f and f_r are fraction of the heat deposited in the front and rear quadrants which were determined by the characteristic radius of the heat source [16]. Q_i is the heat input calculated from the step 1 model by integrating the heat flux distributed in the double-ellipsoidal heat source over the area. l is the lag factor.

In the level-set method used in step 2, the criterion for distinguishing the liquid and gaseous phases is defined as level-set variable ϕ, where ϕ is zero for the gaseous state and 1 for the liquid state. Here, ϕ continuously changes between zero and 1 in the transition layer at the gas–liquid interface. In this instance, the sum of the gas and liquid fractions is always 1. Therefore, the properties of the transition layer at the gas–liquid interface linearly changes according to the value of ϕ between the properties of gas and liquid. The relationship between the fluid flow and moving interface is expressed as follows [9]:

$$\frac{\partial\phi}{\partial t} + \nabla\cdot(\phi\boldsymbol{u}) = \gamma_{ls}\nabla\cdot\left(\epsilon_{ls}\nabla\phi - \phi(1-\phi)\frac{\nabla\phi}{|\nabla\phi|}\right) \tag{8}$$

where γ_{ls} is the reinitialization speed and ϵ_{ls} is the interface thickness controlling parameter.

The pressure applied to the free surface of the molten pool in step 2 is calculated by dividing the pressure acting on the base metal surface of the step 1 model by the grid size in the z-direction [17]. The shear force $\boldsymbol{\tau}$ [18] and the surface tension $\boldsymbol{F_{ST}}$ are calculated as follows:

$$\boldsymbol{\tau} = \mu_g\frac{\partial\boldsymbol{u_i}}{\partial z} \tag{9}$$

$$\boldsymbol{F_{ST}} = \left(\boldsymbol{n}\kappa + \left(I-\boldsymbol{n}\cdot\boldsymbol{n}^T\right)\nabla\gamma\right)\boldsymbol{\delta}(\phi) \tag{10}$$

where μ_g is the dynamic viscosity of argon, $\boldsymbol{u}_i$ is the velocity component in the x or y direction, κ is the curvature, and γ is the surface tension coefficient, which is a function of temperature. Previously reported surface tension coefficient of the Fe-S system considering the effect of the surface active components was applied [19].

In the step 2 model, the governing equations of the level-set method were initialized to set the initial location of the level-set function ϕ, which varies smoothly across the initial liquid–gas interface [20]. For solving the governing equations of the step 2 model, i.e. heat transfer, fluid flow and level-set method, the same solver as in step 1 model is applied.

3. Experimental setup

To verify the simulation model, tandem and H-tandem arc welding experiments were performed using a high-speed camera to capture images of the arc behavior of each process. Fig. 2 displays the schematic of the H-tandem arc welding experiment. Nanomatic 650 (Rexwell, Korea) and Wavematic 500 (Hyundai Welding, Korea) welding machines were used in the leading and trailing parts, respectively. The tigSpeed wire feeder (EWM AG, Germany) with the reverse-polarity was used for hot wire feeding. E71T-1C flux-cored wires (KISWEL, Korea) were used as leading and trailing electrodes, and the ER70S-3 solid wire (KISWEL, Korea) was used as the hot wire. The size of the AH36 base metal used was 200 × 80 × 15 *mm*. Argon was used as the shielding gas for the

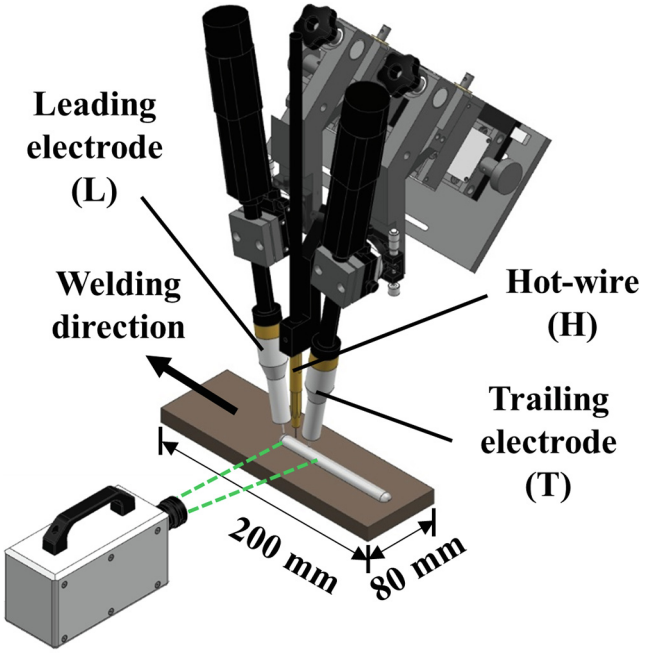

Fig. 2. Schematic of the welding experiment of the H-tandem process.

leading and trailing nozzles, and its flow rate was 18 L/min. Phantom Miro LC 310 (Vision Research, USA), a high-speed camera, was used to observe arc geometry. The amount of light coming into the camera sensor was adjusted and noise was controlled using an 810 nm bandpass filter, a neutral density filter, and an ultraviolet filter. The welding experiment was performed under the same process conditions as the simulation model, and the experimental results were compared with those of numerical analysis using the cross-section macro images of the weldments.

4. Result and discussion

4.1. Electromagnetic forces

Fig. 3 displays a comparison of the electromagnetic force (green arrow) and plasma arc temperature (contour) in step 1 between the (a) tandem and (b) H-tandem processes. The leading arc is deflected in the opposite welding direction, and the trailing arc is in the welding direction in the tandem process. This phenomenon was caused by the difference in the electromagnetic force generated on the left and right sides of the electrodes. As illustrated in Fig. 3(a), the maximum electromagnetic forces on the left and right sides of the leading arc ($F_{L,L}$ and F_{LR}) were 5.22×10^5 and 2.82×10^5 N/m^3, and the maximum electromagnetic forces acting on the left and right sides of the trailing arc ($F_{T,L}$ and $F_{T,R}$) were 1.81×10^5 and 4.62×10^5 N/m^3, respectively, in the tandem process. In the tandem process, the difference in the maximum electromagnetic force between the left and right sides of each electrode is approximately $2.40 \times 10^5 N/m^3$ for the leading electrode and $2.81 N/m^3$ for the trailing electrode. By contrast, in the H-tandem process, as displayed in Fig. 3(b), the differences in maximum electromagnetic force were 1.08×10^5 and $0.78 \times 10^5 N/m^3$ for the leading and trailing electrodes, respectively, which were smaller than those for the tandem process because the attraction between the tandem electrodes was reduced by the reverse-polarity hot wire in the H-tandem process. Because the electromagnetic force is the dominant driving force for the arc flow, the arc deflection in the H-tandem process was lower than that in the tandem process. Furthermore, the direction and magnitude of the electromagnetic force acting on the molten pool exhibit patterns similar to the behavior of the electromagnetic force under each electrode.

Fig. 4 displays a comparison of the trailing arc deflection observed using the high-speed camera between the tandem and H-tandem processes. The deflection angle of the arc generated at the trailing electrode was compared because observing the trailing arc that acted at a higher position was easier than observing the leading arc because of the difference in CTWD. To measure the arc deflection angle, arc center line (black dashed line) was obtained using two tangent lines (red dashed line) to the left and right sides of the arc near the electrode tip with respect to the xz-plane. The arc deflection angle was defined as the angle between the arc center line and the line vertical to the base metal. The observed arc deflection angles of the trailing arc were 24.74° and 11.64° for the tandem and H-tandem processes, respectively. These angles were similar to the arc deflection angles in the simulation results.

Fig. 5 displays the flow rate of gas in the arc region in the tandem and H-tandem processes. The maximum flow rates in the coaxial direction of the leading electrode in the leading arc region, U_L, were 44.75 and 53.44 m/s for the tandem (Fig. 5(a)) and H-tandem processes (Fig. 5(b)), respectively. The maximum flow rate in the

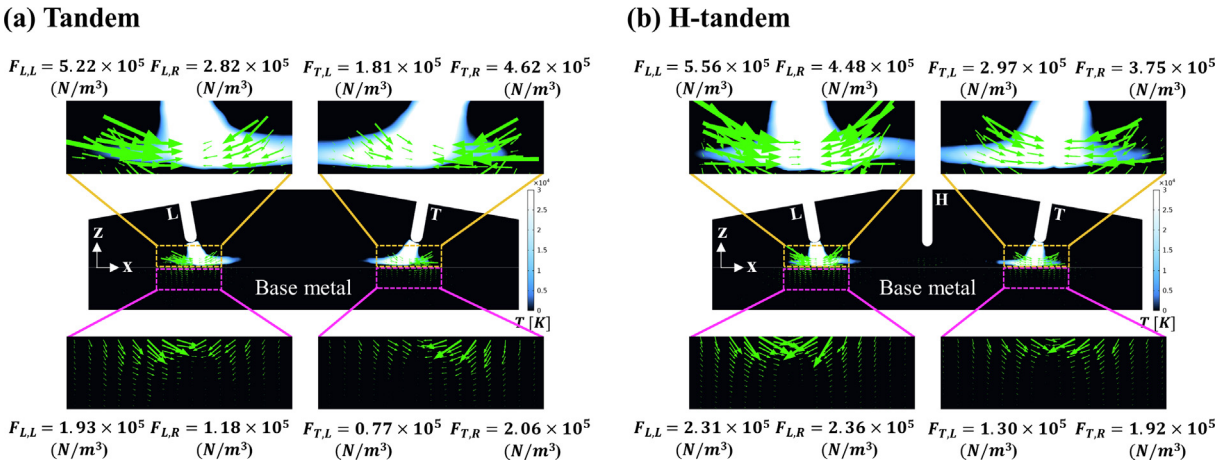

Fig. 3. Electromagnetic force (green arrow) and plasma arc temperature (contour) calculated in the step 1 model: (a) tandem; (b) H-tandem process. (For interpretation of the references to colour in this figure legend, the reader is referred to the web version of this article.)

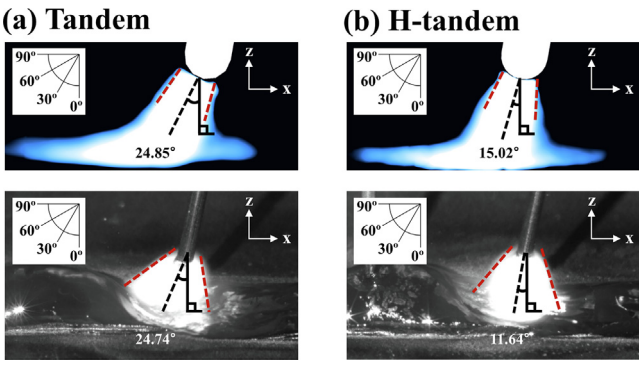

Fig. 4. Observed trailing arc deflection using a high-speed camera: (a) tandem; (b) H-tandem process.

co-axial direction of the trailing electrode in the trailing arc region, U_T, were 40.89 and 49.20 m/s for the tandem and H-tandem processes, respectively. The maximum flow rate in the co-axial direction at each electrode varied depending on the electromagnetic force generated in the tandem and H-tandem processes. As shown in Fig. 5, in the tandem process, the strong flow headed towards the inside from the outside of the two electrodes was generated because of the arc deflection caused by the considerable difference in the electromagnetic force between the left and right sides of each electrode. However, the flow rate of gas in the co-axial direction in the H-tandem process was higher than that in the tandem process because the arc deflection was reduced by the hot wire. This fluid flow considerably influenced the arc pressure and surface shear force.

4.2. Heat transfer

Table 4 lists the geometry parameters of the double-ellipsoidal heat sources used in the two processes. The values of the heat input Q_i which were calculated by the method mentioned in Section 2.2, were 5,023 and 2,489 W for the leading and trailing regions in the tandem process. The corresponding values of heat input were 5,998 and 2,982 W in the H-tandem process. In the H-tandem process, a heat input of 795 W was added to the hot wire region. In the two welding processes, the difference in the heat input between the leading and trailing regions occurred because of the difference in the CTWD.

4.3. Surface forces

Fig. 6 displays the pressure and surface shear force acting on the base metal surface in step 1. The maximum pressures in the leading and trailing regions (p_L and p_T) of the H-tandem process were 686.81 and 390.34 Pa, respectively, which were higher than those of the tandem process (526.10 and 375.03 Pa). The maximum surface shear forces in the x-axis direction at the leading and trailing electrodes ($S_{L,x}$ and $S_{T,x}$) and in the y-axis direction ($S_{L,y}$ and $S_{T,y}$) were also higher in the H-tandem process than those in the tandem process. These results were attributed to the flow rate in the co-axial direction of each electrode in the H-tandem process being higher than that used in the conventional tandem process (Fig. 5). This phenomenon results in strong fluid flows in the vertical downward and horizontal directions on the base metal surface. Furthermore, the surface shear force was balanced between the left and right sides of each electrode in the H-tandem process because the fluid flow in the horizontal direction headed towards the inside from the outside of the two electrodes decreased because of the decrease in arc deflection.

4.4. Molten pool behavior

Fig. 7 illustrates the results of applying the analysis results of step 1 to step 2 (t = 2 s), combined with the level-set method as the volume force and boundary conditions, in the H-tandem process. Fig. 7(a) and Fig. 7(c) displays the enlarged views of the leading and trailing arc regions, respectively. The pressure and surface shear force functions as boundary conditions on the base metal surface defined by the level-set method while moving in the welding direction at the interface between gas and liquid metal, and the electromagnetic force functions as the volume force on the entire molten pool. At 2 s after the start of welding, the trailing electrode passed the initial position of the leading electrode, and the molten pool was stabilized. The constant geometry of the molten pool was then maintained. Considerable changes in the free surface of the molten pool occurred because of the pressures in the leading and trailing arc regions. The deepest penetration occurred in the Fig. 7(c) region, in which melting by the leading arc was followed by additional melting by the trailing arc.

Fig. 8 presents a comparison of the flow of the molten pool between the tandem and H-tandem processes. For both the tandem (Fig. 8(a)) and H-tandem processes (Fig. 8(b)), the flow between the leading and trailing electrodes was generated by the travel angle of the two electrodes. In the molten pool of the tandem process, in particular, deep penetration could not be generated because of the large electromagnetic force towards the inside from the outside of the two electrodes. In the tandem process, the deepest penetration occurred in the leading region where the high current was applied, and the penetration depth gradually decreased until the trailing region. The penetration depth increased again in the trailing region, but it was shallower than that in the leading region. However, in the H-tandem process, flow in the depth direction occurred in the molten pool region under the hot wire because of the change in the direction of electromagnetic force. Accordingly, for the molten pool of the H-tandem process, the deep penetration in the leading region was maintained until the trailing region, and penetration was deeper than that in the leading region because of the pressure of the trailing region. These results can be confirmed through the cross-sections of actual welding specimens to be described later.

Fig. 9 displays the width and flow rate on the free surface of the molten pool. The maximum molten pool widths in the leading arc region, w_L, were 7.38 and 7.68 mm for the tandem (Fig. 9 (a)) and H-tandem (Fig. 9 (b)) processes, respectively. The maximum widths of the molten pool in the trailing arc region, w_T, were 6.20 and 7.94 mm for the tandem and H-tandem processes. The

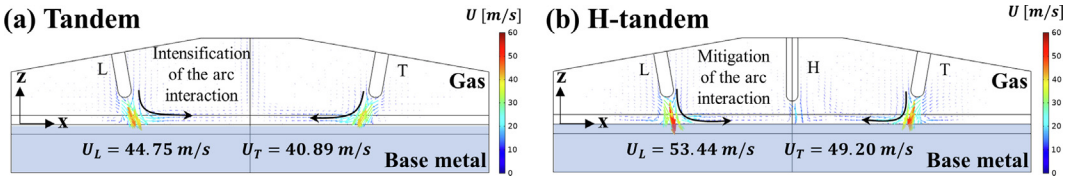

Fig. 5. Flow rate of gas in the arc region: (a) tandem; (b) H-tandem process.

Table 4
Geometry parameters of double-ellipsoidal heat sources.

	Tandem		H-tandem		
	L	T	L	H	T
$r_b[mm]$	4.0	8.4	7.0	6.0	9.5
$r_c[mm]$	2.3	1.0	2.5	1.5	1.0
$r_{af}[mm]$	9.0	15.0	9.5	3.0	15.0
$r_{ar}[mm]$	12.0	9.0	9.0	10.0	10.0
f_f	0.86	1.25	1.03	0.46	1.2
f_r	1.14	0.75	0.97	1.54	0.8

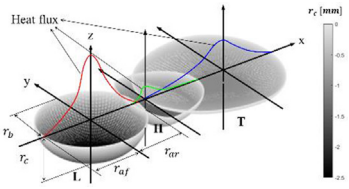

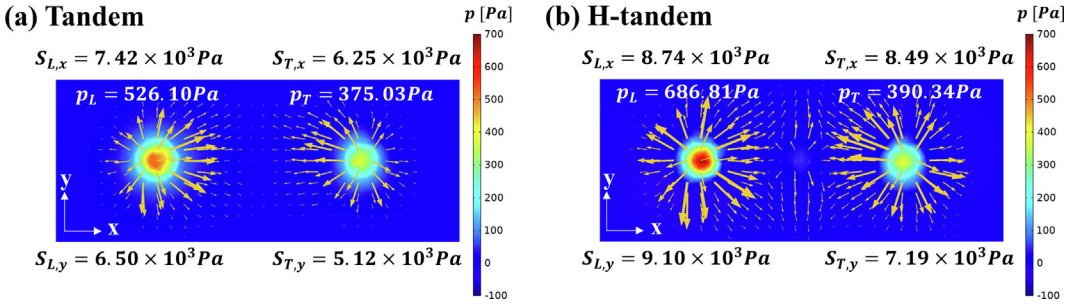

Fig. 6. Pressure (contour) and surface shear force (yellow arrow) acting on the base metal surface (xy-plane): (a) tandem; (b) H-tandem process. (For interpretation of the references to colour in this figure legend, the reader is referred to the web version of this article.)

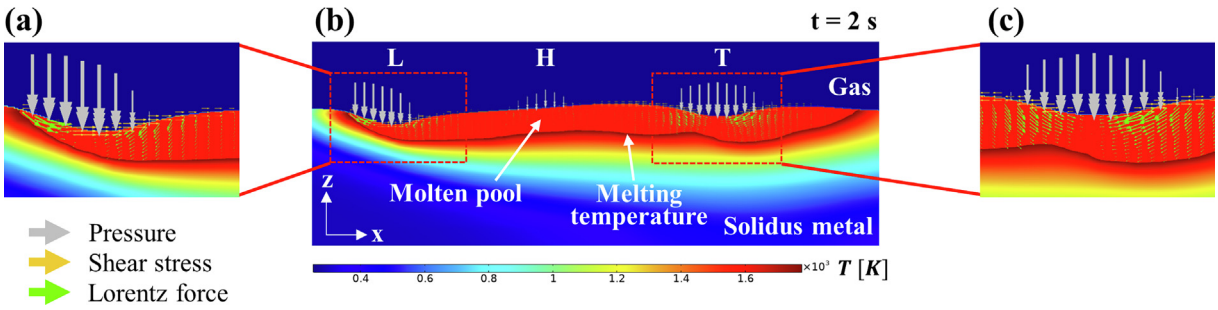

Fig. 7. (b) Results of applying the analysis results of the step 1 model to the step 2 model, combined with the level-set method as volume force and boundary conditions, in the H-tandem process, and the magnified view of the (a) leading arc region and (c) trailing arc region.

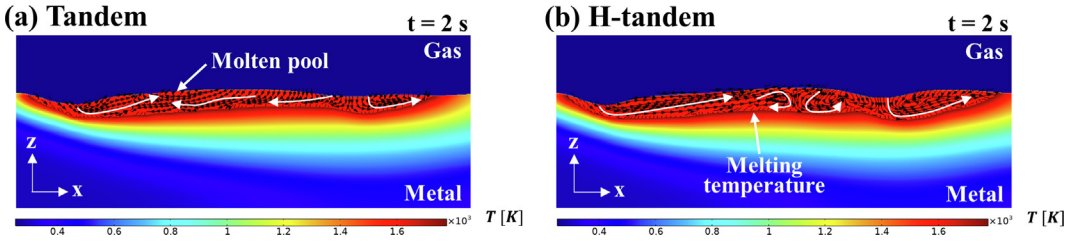

Fig. 8. Flow of the molten pool: (a) tandem; (b) H-tandem process.

leading and trailing molten pool regions were narrower and shorter in the tandem process than those in the H-tandem process because larger surface shear force occurred in the H-tandem process due to a reduction in arc interaction, which induced strong outward flow. The maximum flow rates on the free surface of the molten pool, U_{max}, were 0.155 and 0.223 m/s for the tandem and H-tandem processes. The H-tandem process exhibited higher U_{max} because the pressure acting on the free surface of the molten pool was larger. These results can also be confirmed through the cross-sections of welding specimen to be described later.

Fig. 10 presents a comparison of the cross-sections obtained from the tandem and H-tandem welding experiments with the yz-plane results of both numerical models at 2 s. The experiment results revealed that the penetration depth of the H-tandem process, d, increased by approximately 0.4 mm compared to that of the tandem process (1.440 mm), and the molten pool width, w, increased by approximately 0.2 mm compared with 3.912 mm. Differences between the experiment and simulation results occurred because the mass flow by the droplet transfer and the force caused by the droplet collision were not considered in the developed model. However, droplet transfer in the model causes huge computational load. Therefore, droplet transfer was neglected in order to efficiently achieve the comparison of the arc and molten pool behaviors in the tandem and H-tandem processes which is the

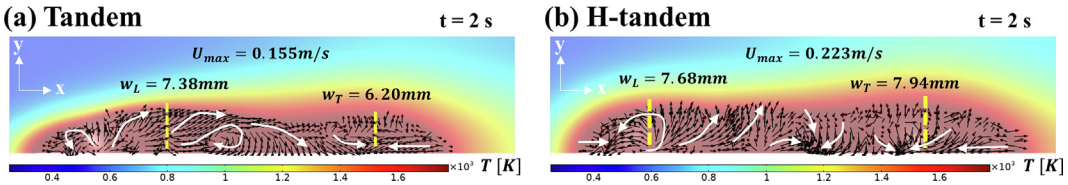

Fig. 9. Width and flow rate on the free surface of the molten pool: (a) tandem; (b) H-tandem process.

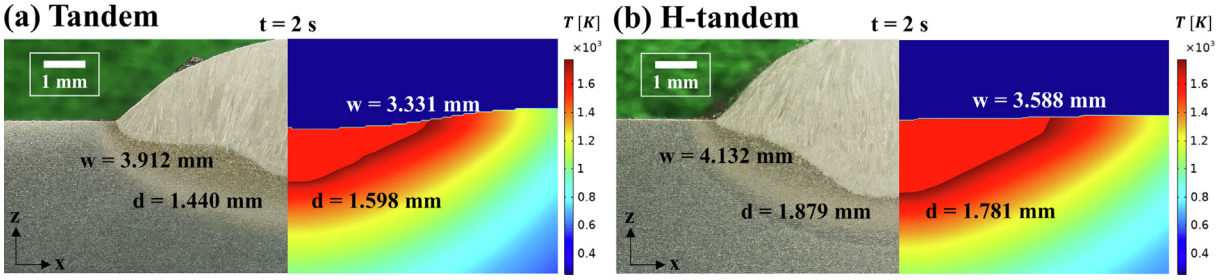

Fig. 10. Verification of the analysis model using weld cross-sections: (a) tandem; (b) H-tandem process.

main purpose of this study. The developed model accurately simulated the tandem and H-tandem molten pool geometry even though the droplet transfer was ignored.

5. Conclusion

In this study, a numerical model of the H-tandem process, in which reverse-polarity hot wire is added between the two electrodes of the tandem process, was developed. The main results can be summarized as follows:

(1) A 3D numerical model of the H-tandem process, in which MHD analysis that considers electromagnetic force, heat transfer, and fluid flow is combined with the level-set method to calculate the free surface of the molten pool, was developed to analyze the arc and molten pool behavior mechanisms of the tandem and H-tandem processes. The developed model consists of step 1, in which the forces and heat acting on the arc and molten pool are calculated, and step 2, in which the behavior of the molten pool is calculated through the forces and heat acting on its free surface. The newly developed two-step model helps not only explain the arc and the molten pool behavior well but also reduce the computation time.

(2) The arc and molten pool behavior mechanisms of the tandem and H-tandem processes were analyzed using the developed model. While two arcs were deflected toward each other by the electromagnetic force generated from each electrode in the tandem process, arc deflection was reduced by reverse-polarity hot wire in the H-tandem process compared to that in the tandem process. Therefore, the downward flow in the co-axial direction of each electrode became faster in the arc region, and the arc pressure, surface shear force, and heat input acting on the molten pool increased. This result considerably affected the depth and width of the molten pool. The arc pressure and surface shear force were the major forces affecting the behavior of the molten pool, and the width and depth of the molten pool were larger in the H-tandem process than in the tandem process.

Declaration of Competing Interest

The authors declare the following financial interests/personal relationships which may be considered as potential competing interests: Seung Hwan Lee reports financial support was provided by Korea Institute of Energy Technology Evaluation and Planning. Seung Hwan Lee reports financial support was provided by Korea Evaluation Institute of Industrial Technology.

Acknowledgments

Funding: This work was supported by the Korea Institute of Energy Technology Evaluation and Planning (KETEP) and the Ministry of Trade, Industry & Energy (MOTIE) of the Republic of Korea (No. 20217710100010), the Korea Evaluation Institute of Industrial Technology (KEIT) grant funded by the Korean government (MOTIE) (No. 20014796).

References

[1] K. Park, H. Jeong, S. Baek, D.-Y. Kim, M.-J. Kang, J. Cho, Turbulent molten pool analysis of tandem GMA automotive steel sheet welding, Int. J. Heat. Mass. Transfer 129 (2019) 1–6, https://doi.org/10.1016/j.ijheatmasstransfer.2018.09.046.

[2] J. Pu, S. Wu, Q. Hu, Y. Wang, Effect of welding current on arc behavior in tandem GMAW, Int. J. Mod. Phys. B 33 (2019) 1940036, https://doi.org/10.1142/S0217979219400368.

[3] M. Schnick, G. Wilhelm, M. Lohse, U. Fuessel, A. Murphy, Three-dimensional modelling of arc behaviour and gas shield quality in tandem gas–metal arc welding using anti-phase pulse synchronization, J. Phys. D: Appl. Phys. 44 (2011), https://doi.org/10.1088/0022-3727/44/18/185205 185205.

[4] H. Arita, T. Morimoto, S. Nagaoka, T. Nakano, Development of advanced 3-electrode MAG high-speed horizontal fillet welding process, Weld. World 53 (2009) 35–43, https://doi.org/10.1007/BF03266713.

[5] Y. Yokota, H. Shimizu, S. Nagaoka, K. Ito, H. Arita, Development and application of the 3-electrode MAG high-speed horizontal fillet welding process, Weld. World 56 (2012) 43–47, https://doi.org/10.1007/BF03321144.

[6] D.Y. Lee, L. Leifsson, J.-Y. Kim, S.H. Lee, Optimisation of hybrid tandem metal active gas welding using Gaussian process regression, Sci. Technol. Weld. Join. 25 (2020) 208–217, https://doi.org/10.1080/13621718.2019.1666222.

[7] D. Wu, J. Huang, L. Kong, X. Hua, M. Wang, Coupled mechanisms of arc, weld pool and weld microstructures in high speed tandem TIG welding, Int. J. Heat. Mass. Transfer. 154 (2020), https://doi.org/10.1016/j.ijheatmasstransfer.2020.119641 119641.

[8] Y. Ogino, Y. Hirata, J. Kawata, K. Nomura, Numerical analysis of arc plasma and weld pool formation by a tandem TIG arc, Weld. World. 57 (2013) 411–423, https://doi.org/10.1007/s40194-013-0040-8.
[9] D. Wang, H. Lu, Numerical analysis of internal flow of molten pool in pulsed gas tungsten arc welding using a fully coupled model with free surface, Int. J. Heat. Mass. Transfer 165 (2021), https://doi.org/10.1016/j.ijheatmasstransfer.2020.120572 120572.
[10] S. Cadiou, M. Courtois, M. Carin, W. Berckmans, 3D heat transfer, fluid flow and electromagnetic model for cold metal transfer wire arc additive manufacturing (Cmt-Waam), Addit. Manuf. 36 (2020), https://doi.org/10.1016/j.addma.2020.101541 101541.
[11] Z. Rao, J. Hu, S. Liao, H.-L. Tsai, Modeling of the transport phenomena in GMAW using argon–helium mixtures. Part I-The arc, Int. J. Heat. Mass. Transfer 53 (2010) 5707–5721, https://doi.org/10.1016/j.ijheatmasstransfer.2010.08.009.
[12] W. Wang, M. Rong, A.B. Murphy, Y. Wu, J.W. Spencer, J.D. Yan, M.T. Fang, Thermophysical properties of carbon–argon and carbon–helium plasmas, J. Phys. D: Appl. Phys. 44 (2011), https://doi.org/10.1088/0022-3727/44/35/355207 355207.
[13] S. Cadiou, M. Courtois, M. Carin, W. Berckmans, P. Le Masson, Heat transfer, fluid flow and electromagnetic model of droplets generation and melt pool behaviour for wire arc additive manufacturing, Int. J. Heat. Mass. Transfer. 148 (2020), https://doi.org/10.1016/j.ijheatmasstransfer.2019.119102 119102.
[14] Y. Zhao, H. Chung, Influence of power source dynamics on metal and heat transfer behaviors in pulsed gas metal arc welding, Int. J. Heat. Mass. Transfer 121 (2018) 887–899, https://doi.org/10.1016/j.ijheatmasstransfer.2018.01.058.
[15] J. Goldak, A. Chakravarti, M. Bibby, A new finite element model for welding heat sources, Metall. Trans. B 15 (1984) 299–305, https://doi.org/10.1007/BF02667333.
[16] K. Sripriyan, M. Ramu, P.R. Thyla, K. Anantharuban, Weld bead characterization of flat wire electrode in gmaw process part II: a numerical study, J. Mech. Sci. Technol. 35 (2021) 2615–2622, https://doi.org/10.1007/s12206-021-0532-1.
[17] T. Li, C. Wu, Numerical simulation of plasma arc welding with keyhole-dependent heat source and arc pressure distribution, Int. J. Adv. Manuf. Technol. 78 (2015) 593–602, https://doi.org/10.1007/s00170-014-6685-7.
[18] X. Wang, D. Fan, J. Huang, Y. Huang, Numerical simulation of arc plasma and weld pool in double electrodes tungsten inert gas welding, In. J. Heat. Mass. Transfer. 85 (2015) 924–934, https://doi.org/10.1016/j.ijheatmasstransfer.2015.01.132.
[19] P. Sahoo, T. DebRoy, M. McNallan, Surface tension of binary metal—surface active solute systems under conditions relevant to welding metallurgy, Metall. Trans. B 19 (1988) 483–491, https://doi.org/10.1007/BF02657748.
[20] A. Ikram, H. Chung, Numerical simulation of arc, metal transfer and its impingement on weld pool in variable polarity gas metal arc welding, J. Manuf. Process. 64 (2021) 1529–1543, https://doi.org/10.1016/j.jmapro.2021.03.001.
[21] J.-Y. Kim, D.Y. Lee, J. Lee, S.H. Lee, Parameter optimization of hybrid-tandem gas metal arc welding using analysis of variance-based Gaussian process regression, Met. 11 (2021) 1087, https://doi.org/10.3390/met11071087.